Superconducting and Fermi Surface Properties of a Valence Fluctuation Compound $CeIr_2$

Omasa, Kazuyuki ; Komoda, Takuya ; Nakamura, Yusuke ; Matsuoka, Eiichi ; Kotegawa, Hisashi ; Tou, Hideki ; Sakurai, Takahiro ; Ohta, Hitoshi …

(Citation)
Journal of the Physical Society of Japan,93(3):034704

(Issue Date)
2024-03-15

(Resource Type)
journal article

(Version)
Accepted Manuscript

(URL)
https://hdl.handle.net/20.500.14094/0100491787

Superconducting and Fermi Surface Properties of a Valence Fluctuation Compound $CeIr_2$

Kazuyuki Omasa[1], Takuya Komoda[1], Yusuke Nakamura[1], Eiichi Matsuoka[1],
Hisashi Kotegawa[1], Hideki Tou[1], Takahiro Sakurai[2], Hitoshi Ohta[1, 3], Ai Nakamura[4],
Yoshiya Homma[4], Dai Aoki[4], Daisuke Satoh[5], Mitsuhiro Yoshida[6], Sanu Mishra[7],
Ilya Sheikin[7], Hisatomo Harima[1], and Hitoshi Sugawara[1*]

[1]*Graduate School of Science, Kobe University, Kobe 657-8501, Japan*
[2] *Research Facility Center for Science and Technology, Kobe University, Kobe 657-8501, Japan*
[3] *Molecular Photoscience Research Center, Kobe University, Kobe 657-8501, Japan*
[4] *Institute for Materials Research, Tohoku University, Oarai, Ibaraki 311-1313, Japan*
[5] *Research Institute for Measurement and Analytical Instrumentation, AIST, Tsukuba 305-8568, Japan*
[6] *Accelerator laboratory, KEK, Tsukuba 305-0801, Japan*
[7] *Laboratoire National des Champs Magnétiques Intenses (LNCMI-EMFL), CNRS, UGA, 38042 Grenoble, France*

(Received)

$CeIr_2$ was reported as a valence fluctuation compound with a superconducting transition temperature of ~0.3 K. To investigate its electronic and superconducting properties, we measured the electrical resistivity, magnetic susceptibility, and de Haas-van Alphen (dHvA) effect at low temperatures cooled to ~30 mK and in high magnetic fields up to 36 T. The upper critical field ($\mu_0 H_{c2}$ = 0.23 T) determined by the electrical resistivity under the magnetic field and the electron–phonon coupling constant (λ_{ep} = 0.39) estimated from the Debye temperature suggested a weak-coupling BCS-type superconductivity. The dHvA effect measurements mapped the Fermi surface in detail. The dHvA branches with the frequencies of F = 122–2180 T and the effective masses of m_c^* = 0.83–2.4 m_0 (m_0: rest mass of an electron) were observed. These were reasonably explained by the band-structure calculation based on the full potential linearized augmented-plane-wave method within the local density approximation.

1. Introduction

Rare-earth intermetallic compounds, RX_2 (R: rare-earth element, X: transition metal element), crystallize into a cubic Laves-phase structure ($MgCu_2$-type, $Fd\bar{3}m$, No. 227).[1)] Most RX_2 compounds with a non-magnetic R (Sc, Y, and La) become superconductors, whereas those with magnetic R (Nd, Pr, and Gd) show ferromagnetism at low temperatures. Ce-based compounds, such as $CeCo_2$, $CeRu_2$, $CeRh_2$, and $CeIr_2$, have a non-magnetic ground state and no crystalline field effect. In other words, these materials are classified as valence fluctuation compounds. $CeIr_2$ exhibits a weakly enhanced Sommerfeld coefficient (γ = 20–28 mJ/K^2mol) and bulk superconductivity below the superconducting transition temperature (T_c) of ~0.3 K.[2,3] Thus, the contribution of 4*f*-electrons to the superconductivity, such as affording a possible unconventional superconductivity, is of significant interest. Additionally, $CeIr_2$ attracts considerable attention as a particularly suitable material for photocathodes because of its high quantum efficiency.[4] However, its detailed physical properties have not been reported because of the difficulty in growing high-quality single crystals. It is essential to study its electronic state to understand the physical properties and the origin of the good performance of the application.

Recently, we have successfully grown high-quality single crystals of $CeIr_2$ and investigated its electrical resistivity and specific heat.[3] However, the detailed superconducting properties have not been investigated because of the relatively low T_c. Further, we have successfully observed the de Haas-van Alphen (dHvA) oscillations for the first time in magnetic fields below 17 T. However, only one weakly angular-dependent dHvA frequency branch has been observed, whereas band-structure calculations have predicted rather complex Fermi surfaces with many orbits.[3,5] In this work, we measured the electrical resistivity, magnetic susceptibility, and dHvA effect at temperatures lower and magnetic fields higher than those of our previous works using high-quality single crystals. The experimental results are compared with the band-structure calculation based on the full potential linearized augmented-plane-wave (FLAPW) method within the local density approximation (LDA).

2. Experimental Details

The single crystals of $CeIr_2$ and the reference compound, $LaIr_2$, were grown by a Czochralski pulling method using a tetra-arc furnace, as described in previous reports.[3,6] Most of the samples used in the experiments were annealed at 900°C under a high vacuum; however, for the superconducting properties, the as-grown samples were used to avoid the effect of the filament superconducting impurity phase, as described later. Figure 1(a) shows a photograph of a typical single crystal of $\mathrm{CeIr_2}$. The phase purity was confirmed by powder X-ray diffraction (XRD), as shown in Fig. 1(b). No impurity phase was detected in both as-grown and annealed samples within the experimental accuracy. The lattice constants of $\mathrm{CeIr_2}$ and $\mathrm{LaIr_2}$ determined by the single-crystal XRD were 7.5807(4) and 7.6936(3) Å, respectively, which were consistent with those of the previous report.$^{1)}$ The crystallographic axes of the samples were confirmed by a back-reflection Laue method, as shown in Fig. 1(c). The electrical resistivity was measured by a conventional four-probe DC method in a top-loading dilution refrigerator cooled to ~30 mK with a 15 T superconducting magnet. Further, we utilized the four-probe AC method for the electrical resistivity measurement in an adiabatic demagnetization refrigerator cooled to 0.17 K under zero field, whose results were the same as those of the DC one. The magnetic susceptibility was measured by a pulling method in a superconducting quantum interference device magnetometer (Quantum Design, MPMS). The dHvA signals were measured by a standard field-modulation method in a top-loading dilution refrigerator cooled to ~30 mK with a 15 T superconducting magnet. Further, they were measured by a magnetic-torque method using a capacitive cantilever at low temperatures cooled to ~50 mK using a top-loading dilution refrigerator in static magnetic fields up to 36 T at Laboratoire National des Champs Magnétiques Intenses in Grenoble.

3. Results and Discussion

Figure 2(a) shows the temperature dependences of the electrical resistivity, $\rho(T)$, in both as-grown and annealed samples of $\mathrm{CeIr_2}$ for the current along the crystal axis J // [100]. These results above 0.5 K are the same as those of the previous report.$^{3)}$ The $\rho(T)$s in both samples decreased with decreasing temperature from room temperature, exhibiting convex curvature. Below ~15 K, the $\rho(T)$s were T^2 dependent followed by the saturating tendency below ~7 K. Assuming the relation $\rho(T) = \rho_0 + AT^2$ between 4 and 15 K, where ρ_0 is the residual resistivity and A is the coefficient of electron–electron scattering, we can estimate ρ_0 and A to be 32 (5.1) μΩcm and 2.5 (3.5) × 10^{-3} μΩcm/K^2 for the as-grown (annealed) sample, respectively. These A-values follow the Kadowaki–Woods relation,[7)] considering the Sommerfeld coefficient γ = 20–28 mJ/(K^2mol). The residual resistivity ratio (RRR = ρ_{297K}/ρ_0) of the as-grown sample is 3, whereas that of the annealed one is 18.

As shown in the inset of Fig. 2(a), the $\rho(T)$ in the annealed sample in $CeIr_2$ shows superconductivity below ~3.5 K; however, the superconductivity is not a bulk property. The superconductivity is suspected to be caused by filaments or traces of impurity phase, most probably $CeIr_3$ ($PuNi_3$-type rhombohedral structure, D_{3d}^{5}, No. 166) which is precipitated by annealing. The bulk superconductivity below T_c = 3.4 K of $CeIr_3$ was reported by Sato et al.[8)] A similar annealing effect was also observed in $LaIr_2$ (not shown here); the filament superconductivity of $LaIr_3$ was observed at ~2.5 K in the annealed sample, whereas the bulk superconductivity in $LaIr_2$ was observed at ~0.42 K.[6,9)]

To avoid the effect of the impurity phase, we measured $\rho(T)$ in the as-grown sample at temperatures down to ~30 mK and observed the intrinsic superconducting transition of $CeIr_2$ at T_c = 0.30 K, which was defined as the midpoint of resistivity drop. The transition temperature is consistent with that determined by the specific heat measurement.[3)] Combined with the Debye temperature ($\Theta_{\mathrm{D}} = 232$ K) determined by the specific heat measurement, the electron–phonon coupling constant (λ_{ep}) can be estimated using a McMillan formula: $T_{\mathrm{c}} = \frac{\Theta_{\mathrm{D}}}{1.45}\exp\left[\frac{1.04(1+\lambda_{\mathrm{ep}})}{\lambda_{\mathrm{ep}}-\mu^*(1+0.62\lambda_{\mathrm{ep}})}\right]$, or more conveniently, $\lambda_{\mathrm{ep}} = \frac{1.04+\mu^*\ln(\Theta_{\mathrm{D}}/1.45T_{\mathrm{c}})}{(1-0.62\mu^*)\ln(\Theta_{\mathrm{D}}/1.45T_{\mathrm{c}})-1.04}$,[10)] where μ^* represents a Coulomb repulsion constant. Assuming a typical value of $\mu^* = 0.13$, we estimate $\lambda_{\mathrm{ep}} = 0.39$, which indicates that the superconductivity of $CeIr_2$ is situated in a weak-coupling regime.

To construct the superconducting H–T phase diagram, we measured the field dependence of the electrical resistivity at selected temperatures below 0.25 K for J // [100] and H // [001], as shown in the inset of Fig. 2(b), where the superconducting upper critical field, H_{c2}, was defined as the midpoint of the resistivity drop. The main panel of Fig. 2(b) shows the H–T phase diagram. The H_{c2} at the lowest temperature of 0.03 K was determined as ~0.22 T, from which we can estimate the coherence length, ξ ~390 Å, using the relation $H_{c2} = \frac{\Phi_0}{2\pi\mu_0\xi^2}$. From our previous work,$^{3)}$ the mean free path, ℓ, was estimated to be ℓ ~1080 Å; therefore, the superconductivity can be considered within the clean limit ($\ell > \xi$). As the origin of the critical field, two pair-breaking mechanisms are known within the weak-coupling BCS theory: the orbital depairing and the paramagnetic effect. The orbital critical field, H_{orb}, can be evaluated based on the Werthamer–Helfand–Hohenberg model.$^{11,12)}$ The model considerably fitted the observed data and yields the critical field at 0 K $\mu_0 H_{\mathrm{orb}}(0) = 0.727\ T_{\mathrm{c}}\ (-d\ \mu_0 H_{\mathrm{c2}}/dT)_{T=T_{\mathrm{c}}} = 0.23$ T within the clean limit. Conversely, the Pauli limit, H_{P}, due to the paramagnetic effect is estimated to be $\mu_0 H_{\mathrm{P}}(0) = 1.83\ T_{\mathrm{c}} = 0.55$ T, which is more than two times larger than that of the observation. These facts suggest that the critical field of $\mathrm{CeIr_2}$ is governed by the orbital limit rather than by the Pauli limit.

Hereafter, we used the annealed samples for the measurements of normal state physical properties because of the better sample qualities, considering the RRR values. Judging from the powder XRD experiments, as shown in Fig. 1(b), the amount of impurity phase of $\mathrm{CeIr_3}$ is negligible. Figure 3 shows the temperature dependences of magnetic susceptibility $\chi(T)$s in both $\mathrm{CeIr_2}$ and $\mathrm{LaIr_2}$ under the magnetic field $\mu_0 H = 0.1$ T for the field along H // [100]. Both magnetic susceptibilities are almost independent of the temperature, particularly at high temperatures, indicating the Pauli paramagnetism of these compounds. The slight increase in $\chi(T)$ with decreasing temperature in both samples is most probably due to the paramagnetic impurity effect. By subtracting the Curie-like contributions, we estimated the Pauli paramagnetic susceptibilities, χ_P, for $\mathrm{CeIr_2}$ and $\mathrm{LaIr_2}$ to be 5.9×10^{-4} and $0.71\ \times 10^{-4}$ emu/mol, respectively. The absolute value of χ_P for $\mathrm{CeIr_2}$ is more than eight times higher than that of $\mathrm{LaIr_2}$, which implies that the large density of states (DOS) at the Fermi level is due to the 4*f*-electrons. Using the χ_P and γ = 20–28 mJ/(K^{2}mol), we estimate the Wilson ratio, $R_{\mathrm{W}} = \frac{\pi^2 k_B^2}{3\mu_B^2}\frac{\chi_P}{\gamma}$, which is the measure of electronic correlations, to be R_{W} = 1.5–2.1. This value is almost comparable to that of the typical heavy fermion systems.$^{13)}$

Next, we show the results of the dHvA experiments on $\mathrm{CeIr_2}$. Figures 4(a) and 4(b) show the typical dHvA oscillations for field angle at $\theta = -2°$ from [100] to [101] and the corresponding fast Fourier transformation (FFT) spectra, respectively. The dHvA-frequency (F), which is expressed as a unit of magnetic field, is proportional to the extremal cross-sectional area, S_F, of the Femi surface with the following relation: $F = c\hbar S_F/(2\pi e)$.[14] Several dHvA signals with F = 122–1560 T were observed, as shown in Fig. 4(b), where the typical signals are labeled as α, β, β', ε, δ, and ζ. The amplitudes of signals β, δ, and ζ are relatively large, whereas those of α, β', and ε are small and only visible in the limited high field ranges, as shown in the inset of Fig. 4(b).

To investigate the Fermi surface (FS) topology, we measured the angular dependence of the dHvA-frequency, as shown in Fig. 5(a). The dHvA-frequency branches, α and δ, were observed for all angular ranges with weak angular dependences, indicating almost spherical FSs, where the δ-branch corresponds to what we observed in our previous work.[3] Owing to the high magnetic fields and the low temperatures, we observed several new dHvA-frequency branches in the present work. Branch α' was observed in the limited angular ranges at $\theta = -45 \sim -16°$ in (100) and $\theta = 28 \sim 59°$ in $(0\bar{1}1)$ with weak angular dependences. Branches β, β', ε, and ζ exhibited some specific angular dependences, whose possible origins will be discussed later. We note here that the angular dependences of $\mathrm{CeIr_2}$ are highly different from those of $\mathrm{LaIr_2}$.[6] This suggests the significant contribution of 4*f*-electrons to the band structure or the itinerant nature of 4*f*-electrons in $\mathrm{CeIr_2}$, which is consistent with the result of the band-structure calculation, as will be mentioned later.

To assign the origin of the dHvA-frequency branches, the band-structure calculation for $\mathrm{CeIr_2}$ was carried out based on the FLAPW method within the LDA. The resultant band structure and its DOS are shown in Figs. 6(a) and 6(b), respectively. The bands mainly consist of Ce-4*f* and Ir-5*d* bands, and the FS consists of three sheets originating from the 41st–43rd bands, as shown in Figs. 7(a)–7(c). The considerable contribution of the Ce-4*f* electrons at Fermi energy (E_F) shows that $\mathrm{CeIr_2}$ is a mixed-valence compound. The total DOS at E_F (= 0.94663 Ry) is 160.015 states/(Ry cell), which corresponds with the γ of 13.87 mJ/(K^{2}mol). As shown in Fig. 7(a), the 41st band constructs one hole FS centered at the Γ point of the first Brillouin zone (1st BZ), whose shape is almost spherical. The 42nd-band constructs hole sheets that consist of a rounded cube centered at the Γ point and twelve distorted ellipsoids that lie across the Σ axes, as shown in Fig. 7(b). The 43rd-band constructs an electron sheet centered at the Γ point, connecting along the <111> directions, as shown in Fig. 7(c). This FS exhibits a hole centered at the Γ point and the six windows along the <100> directions. $\mathrm{CeIr_2}$ is a compensated metal with an equal carrier number of electrons and holes because the primitive cell of the crystal structure consists of two molecules.

Hereafter, let us consider the origin of the dHvA-frequency branches observed in the present experiments. The theoretical angular dependence of the dHvA-frequency obtained by the band-structure calculation is shown in Fig. 5(b). Compared with the theoretical angular dependence, it is evident that branch δ originated from the 41st-band hole FS. Branch α most likely corresponded with the round cube hole FS of the 42nd band, although the absolute value of the dHvA-frequency is approximately 1.5 times larger than that of the theoretical one. Assuming the FSs are spherical, the FS volumes of branches δ and α are estimated to be 0.53% and 1.54% of the volume of the 1st BZ, respectively. Branches β and β' likely correspond with the ellipsoidal FSs of the 42nd-band, whose extremal cross-sectional areas are almost degenerate for the field along the [111] direction. The volume of the ellipsoidal FSs is estimated to be 19.86% of that of the BZ in total. Judging from the angular dependences, branches α', ε, and ζ might originate from the 43rd-band electron FS. Thus, the experimental angular dependences of the dHvA-frequencies are reasonably explained by the band-structure calculation, though the calculated absolute values are slightly smaller than those of the experimental ones. This discrepancy may be improved if we consider the effect of Coulomb correlations between 4f-electrons by applying the LDA+U method; that is a future work.

According to the Lifshitz–Kozevich formula,$^{14)}$ the temperature dependence of the dHvA amplitude, A_{dHvA}, (magnitude of the FFT spectrum) is given by $\ln\{A_{\mathrm{dHvA}}[1 - \exp(-2\lambda m_{\mathrm{c}}^{*}T/H)]/T\} = -\lambda m_{\mathrm{c}}^{*}T/H + \mathrm{const.}$, where λ is a constant, $\lambda = 2\pi^2 c k_{\mathrm{B}}/(e\hbar)$, and

m_c^* is the cyclotron effective mass. From the temperature dependence of the dHvA amplitude (so-called mass plot), as shown in Fig. 8, we estimated the m_c^* for each dHvA-frequency. The estimated m_c^*s compared with the results of the band-structure calculation are summarized in Table I, along with the dHvA-frequencies. The experimental m_c^*s are not considerably large, ranging from 0.83 to 2.4 m_0 (m_0: rest mass of an electron), which are approximately two times larger than those of the theoretical m_c^*s. This is consistent with the enhancement of the γ; the experimental and theoretical γs are 20–28 mJ/(K^{2}mol) and 13.78 mJ/(K^{2}mol), respectively. From the observed dHvA-frequencies and their cyclotron effective masses, we estimated the γ using the relation $\gamma = k_B{}^2Vm^*k_F/(3\hbar^2)$, where V is the molar volume, m^* is the effective mass, and k_F is the caliber of the Fermi sphere: $S_F = \pi k_F{}^2$. The estimated γ-values for the α-, α'-, $\beta(\beta')$-, δ-, and ζ-branches are 0.8, 9.0, 6.5, 0.2, and 1.6 mJ/(K^{2}mol), respectively, and 18 mJ/(K^{2}mol) in total. This value is almost comparable to that estimated from the specific heat measurements. The band-structure calculation predicted the F = 5405 T with the largest m_c^* = 5.792 m_0 of the 43rd-band electron FS for H // [100]; however, we could not observe the corresponding dHvA single in the present experiment. Considering the mass enhancement, the expected m_c^* for this dHvA-frequency should be ~12 m_0, which is observable if we can improve the sample quality.

Finally, we compare the typical physical quantities of CeIr$_2$ with those of CeRu$_2$, CeCo$_2$, and CeRh$_2$, as shown in Table II,[2,3,15–19] which might be helpful to understand the difference in those superconducting properties. CeRh$_2$, in which the superconductivity has not been observed down to 0.2 K so far, [2] is listed for the reference. CeRu$_2$ exhibits the highest T_c of 6.3 K, which is the highest among all Ce-based intermetallic compounds. The most interesting feature of the superconducting properties is the possibility of an anisotropic s-wave superconducting gap, which was demonstrated by nuclear magnetic resonance (NMR), [20] photoemission spectroscopy,[21] and more conclusively, field angle resolved specific heat measurements.[22] CeCo$_2$ also exhibits a relatively high T_c of 1.5 K despite consisting of a magnetic element, Co. Further, this compound was reported as an anisotropic s-wave superconductor by the NMR measurements,[23] and the ferromagnetic spin fluctuation was considered as the gap anisotropy by the specific heat measurements.[17)]

The large variation in the T_c of CeX_2, i.e., 0.3–6.3 K, is evident, although the γ-values are not considerably different among these compounds. This is somewhat notable, considering the BCS theory; T_c is given by $T_c = 1.14\Theta_D \exp\left[\frac{-1}{N(0)V}\right]$, where $N(0)$ is the DOS at the Fermi energy and V is the pairing potential arising from the electron–phonon interaction. Since the Θ_D of $CeRu_2$ is approximately two times smaller than that of $CeIr_2$, whereas the T_c is more than one order larger. The large variation in T_c is explained by the difference in the strength of the electron–phonon couplings. Using the McMillan formula mentioned above, we estimate the electron–phonon coupling constants for $CeRu_2$ and $CeCo_2$ to be 0.80 and 0.59, respectively, which are comparable with the medium value of that of pure Nb ($\lambda_{ep} = 0.82$). Conversely, $\lambda_{ep} = 0.39$ for $CeIr_2$ is close to that of pure Al ($\lambda_{ep} = 0.38$), which is a typical weak-coupling BCS-type superconductor. However, a question arises: what is the microscopic mechanism for the large difference in λ_{ep} depending on the X element? The number of valence electrons in $CeRu_2$ should be different from those of other CeX_2 (X = Co, Rh, and Ir), so let us compare T_c or Θ_D in the same group of the periodic table, i.e., in CeX_2 (X = Co, Rh, and Ir). However, it is also notable that there are no systematic variations in these values with X. Considering that Θ_D is expressed as $\Theta_D = \frac{\hbar\omega_D}{k_B} \propto \frac{1}{\sqrt{M}}$, where ω_D and M are Debye frequency and mass of ions, respectively, the Θ_D should be highest in $CeCo_2$ and should be lowest in $CeIr_2$. But the experimental results show the opposite. This fact suggests that the difference in Θ_D is not simply originated from the difference of M in CeX_2 (X = Co, Rh, and Ir).

It is interesting to discuss from the viewpoint of the difference in the band structures, particularly from the role of 4*f*-electrons, because all these compounds are situated in the valence fluctuation regime and the contribution of the 4*f*-electron is expected to be important for the superconductivity. The systematic band-structure calculations for CeX_2 (X = Co, Ru, and Rh) based on the density functional theory within the LDA were performed by Tanaka et al., [24)] in which the many-body effects were taken into account. The remarkable points of the resultant electronic structures are summarized as follows.

For all CeX_2, the contributions of the 4*f*-components of Ce to DOS (4*f*-DOS) are significant at E_F, however, the shape of the 4*f*-DOS and its relative position to E_F are highly different among these compounds. The main peak of 4*f*-DOS for $CeRu_2$ lies slightly above E_F at ~0.007 Ry, whereas the small peak of 4*f*-DOS exists below E_F at ~0.04 Ry. While the main peak of the 4*f*-DOS of $CeCo_2$ lies relatively far from E_F at above ~0.03 Ry, and the small peak of 4*f*-DOS exists just below E_F. On the other hand, the 4*f*-DOS for $CeRh_2$ exists in both sides of the vicinity of E_F. Tanaka et al. pointed out that the shape of the 4*f*-DOS and the relative position to E_F are important for mass enhancement which was evaluated by $\frac{\gamma_{\mathrm{exp}}}{\gamma_{\mathrm{band}}} - 1$, where γ_{exp} and γ_{band} are the experimental and the calculated Sommerfeld coefficients, respectively. For $CeIr_2$, the total DOS at E_F is almost the same as those of $CeRu_2$ and $CeCo_2$, however, the shape is highly different from those of compounds and rather similar to that of no-superconducting $CeRh_2$. The contributions of the 4*f*-component R_f at E_F are highly different among these compounds; R_f is ~30% in $CeRu_2$ and $CeCo_2$, whereas R_f is ~60% in $CeRh_2$ and $CeIr_2$, indicating higher 4*f* contributions to the band structures or the itinerant natures in $CeRh_2$ and $CeIr_2$. Such a difference in the band structure and the hybridization effect between Ce 4*f*- and X *d*-electrons may be responsible for the large difference in λ_{ep} as well as the difference in the superconductivity in CeX_2.

4. Summary

We measured the electrical resistivity, magnetic susceptibility, and dHvA effect to investigate the electronic and superconducting properties of $CeIr_2$. The superconducting *H*–*T* phase diagram was constructed using the electrical resistivity measurements under the magnetic fields, where the critical temperature $T_c = 0.30$ K and the upper critical field $\mu_0 H_{c2} = 0.23$ T were determined. In the present work, the superconductivity can be explained by the weak-coupling BCS theory with the electron–phonon coupling constant, $\lambda_{\mathrm{ep}} = 0.39$. The magnetic susceptibility is nearly constant at high temperatures, suggesting Pauli paramagnetism. Combined with the γ-value of 28 mJ/K^2mol and the Pauli paramagnetic susceptibility, $\chi_P = 0.71 \times 10^{-4}$ emu/mol, $CeIr_2$ is a weakly correlated electron system. From the dHvA effect measurements, we observed the dHvA branches with the frequencies of F = 122–2180 T and the effective masses of m_c^* = 0.83–2.4 m_0, which were reasonably explained by the band-structure calculation. The large variation in the T_c of CeX_2 was discussed based on the differences in the band structures in the vicinity of the E_F.

Acknowledgment

This work was partly supported by JSPS KAKENHI Grants Nos. JP15H05882, JP15H05884, JP15H05885, 18H04320, 18H04321, and 21K03470.

*E-mail: sugawara@crystal.kobe-u.ac.jp

1) V. B. Compton and B. T. Matthias, Acta Cryst. **12**, 651 (1959).

2) H. Sugawara, T. Yamazaki, J. Itoh, M. Takashita, T. Ebihara, N. Kimura, P. Svoboda, R. Settai, Y. Ōnuki, H. Sato, S. Uji, and H. Aoki, J. Phys. Soc. Jpn. **63**, 1502 (1994).

3) K. Omasa, E. Matsuoka, H. Kotegawa, H. Tou, A. Nakamura, Y. Homma, D. Aoki, D. Satoh, M. Yoshida, T. Takeuchi, H. Harima, and H. Sugawara, JPS Conf. Proc. **30**, 011130 (2020).

4) D. Satoh, T. Shibuya, H. Ogata, M. Tanaka, H. Ikeura-Sekiguchi, R. Kuroda, M. Yoshida, H. Sugawara, and H. Toyokawa, Jpn. J. Appl. Phys. **58**, SIIB10 (2019).

5) T. Maehira, Y. Tatetsu, H. Teruya, and E. Sakai, J. Phys. Soc. Jpn, **81**, SB012 (2012).

6) K. Omasa, E. Matsuoka, H. Kotegawa, H. Tou, A. Nakamura, Y. Homma, D. Aoki, D. Satoh, M. Yoshida, T. Takeuchi, H. Harima, and H. Sugawara, JPS Conf. Proc. **29**, 012012 (2020).

7) K. Kadowaki and S. B. Woods, Solid State Commun. **58**, 507 (1986).

8) Y. J. Sato, A. Nakamura, Y. Shimizu, A. Maurya, Y. Homma, D. Li, F. Honda, and D. Aoki, J. Phys. Soc. Jpn. **87**, 053704 (2018).

9) T. H. Geballe, B. T. Matthias, V. B. Compton, E. Corenzwit, G. W. Hull, Jr., and L. D. Longinotti, Phys. Rev. **137**, A119 (1965).

10) W. L. McMillan, Phys. Rev. **167**, 331 (1968).

11) E. Helfand and N. R. Werthamer, Phys. Rev. **147**, 288 (1966).

12) N. R. Werthamer, E. Helfand, and P. C. Hohenberg, Phys. Rev. **147**, 295 (1966).

13) L. A. Lee, T. M. Rice, J. W. Serene, L. J. Sham, and J. W. Wilkins, Comments Condens. Mater. Phys. **12**, 99 (1986).

14) D. Shoenberg, *Magnetic Oscillations in Metals* (Cambridge University Press, Cambridge, 1984), p. 22.

15) M. Hedo, Y. Inada, E. Yamamoto, Y. Haga, Y. Ōnuki, Y. Aoki, T. D. Matsuda, H. Sato, and S. Takahashi, J. Phys. Soc. Jpn. **67**, 272 (1998).

16) H. Sugawara, H. Sato, T. Yamazaki, N. Kimura, R. Settai, and Y. Ōnuki, J. Phys. Soc. Jpn. **64**, 4849 (1995).
17) Y. Aoki, T. Nishigaki, H. Sugawara, and H. Sato, Phys. Rev. B **55**, 2768 (1997).
18) H. Sugawara, O. Inoue, Y. Kobayashi, H. Sato, T. Nishigaki, Y. Aoki, H. Sato, R. Settai, and Y. Ōnuki, J. Phys. Soc. Jpn. **64**, 3639 (1995).
19) M. Ozawa, M. Yoshizawa, H. Sugawara, and Y. Onuki, Physica B **206 & 207**, 267 (1995).
20) H. Mukuda, K. Ishida, Y. Kitaoka, and K. Asayama, J. Phys. Soc. Jpn. **67**, 2101 (1998).
21) T. Kiss, F. Kanetaka, T. Yokoya, T. Shimojima, K. Kanai, S. Shin, Y. Ōnuki, T. Togashi, C. Zhang, C. T. Chen, and S. Watanabe, Phys. Rev. Lett. **94**, 057001 (2005).
22) S. Kittaka, T. Sakakibara, M. Hedo, Y. Ōnuki, and K. Machida, J. Phys. Soc. Jpn. **82**, 123706 (2013).
23) K. Ishida, H. Mukuda, Y. Kitaoka, K. Asayama, H. Sugawara, Y. Aoki, and H. Sato, Physica B **237-238**, 304 (1997).
24) S. Tanaka, H. Harima, and A. Yanase, J. Phys. Soc. Jpn. **67**, 1342 (1998).

Figure Captions

Fig. 1. (Color online) (a) Photograph of the single-crystal ingot of $CeIr_2$. (b) Comparison of the powder X-ray diffraction patterns between the as-grown and annealed samples, which are well explained by the simulation (calc. for $CeIr_2$) and no impurity phase is identified in both samples. The inset shows the expanded view of the angles between 39 and 40° for the annealed sample, where the main peak of $CeIr_3$ is expected at around 39.75° (calc. for $CeIr_3$), but there is nothing visible except the main peak of $CeIr_2$. (c) Typical back-reflection Laue photograph for [110] direction.

Fig. 2. (Color online) (a) Temperature dependences of electrical resistivity (ρ) at zero field for the as-grown and annealed samples in $CeIr_2$. The inset shows the expanded view below 5 K. (b) Superconducting H–T phase diagram in the as-grown sample. The solid line shows a fitting of the data based on the Werthamer–Helfand–Hohenberg model. The inset shows the field dependences of ρ at selected temperatures below 0.25 K.

Fig. 3. (Color online) Temperature dependences of magnetic susceptibility, χ, under the magnetic field of 0.1 T for the field along [100] in $CeIr_2$ and $LaIr_2$.

Fig. 4. (Color online) (a) Typical dHvA oscillations for field angle at $\theta = -2^\circ$ from [100] to [101] and (b) the corresponding fast Fourier transformation (FFT) spectra in $CeIr_2$. The inset of (b) shows the FFT spectra between 23 and 36 T.

Fig. 5. (Color online) Comparison between (a) the experimental and (b) theoretical angular dependences of the dHvA-frequencies in $CeIr_2$. Solid lines in (a) are guides to the eyes.

Fig. 6. (Color online) (a) Band structure and (b) its density of states of $CeIr_2$. Fermi energy is denoted by E_F.

Fig. 7. (Color online) Femi surface of $CeIr_2$. Greek characters α, α', β, β', δ, ε, and ζ are corresponding to the observed dHvA branches, as shown in Fig. 5(a). The other characters shown in (a) represent the specific points and axes of the first Brillouin zone (1st BZ), where the Γ point (not shown here) is the center of the BZ.

Fig. 8. (Color online) Temperature dependence of the dHvA amplitude, A_{dHvA}, (mass plot) for the α-, β-, β'-, δ-, and ζ-branches for the field along H // [100] in $CeIr_2$. Solid lines represent linear fittings.

Table I. dHvA frequency (F) and the corresponding cyclotron effective mass (m_c^*) in CeIr$_2$ for the field along H // [100], H // [110], and H // [111] compared with the results of the band structure calculation.

		Experimental		Theoretical		
Field direction	Branch	F ($\times 10^2$ T)	m_c^*/m_0	F ($\times 10^2$ T)	m_c^*/m_0	Band
[100]				54.05	5.792	43rd
	α	15.6	2.20 ± 0.03	9.776	0.673	42nd
	β'	13.5	1.71 ± 0.03	10.22	0.775	42nd
	β	7.58	1.9 ± 0.1	5.556	1.593	42nd
	δ	6.75	0.83 ± 0.01	7.446	0.490	41st
	ζ	1.22	1.3 ± 0.1	2.365	1.150	43rd
[110]	α'	21.8	1.0 ± 0.1	21.93	4.044	43rd
	α	15.4	2.14 ± 0.05	12.10	0.971	42nd
	β'	12.0	-	8.902	2.548	42nd
	β	9.37	-	6.846	2.011	42nd
	δ	6.98	1.01 ± 0.01	6.364	0.405	41st
	ζ	1.96	-	4.206	1.236	43rd
[111]				56.52	5.155	43rd
	α'	21.8	2.4 ± 0.2	23.47	5.320	43rd
	β	9.84	-	1.078	0.800	42nd
	δ	6.54	0.87±0.01	6.071	0.385	41st
	ζ	1.49	-			

Table II. Comparison of the superconducting and other physical quantities in CeX_2 (X = Co, Ru, Rh, and Ir). The parenthesis numbers indicate the references.

Physical quantity	$CeIr_2$	$CeRu_2$	$CeCo_2$	$CeRh_2$
T_c (K)	0.30	6.3 (15)	1.5 (17)	< 0.2 (2)
$\mu_0 H_{c2}$ (T)	0.23	5.2 (15)	0.22 (18)	–
γ (mJ/K^2mol)	28 (3)	27 (15)	36 (17)	20 (2)
χ_P (X10^{-4} emu/mol)	5.9	7 (16)	10 (17)	8 (19)
Θ_D (K)	232 (3)	120 (15)	200 (17)	210 (2)
λ_{ep}	0.39	0.80	0.59	< 0.38 (2)

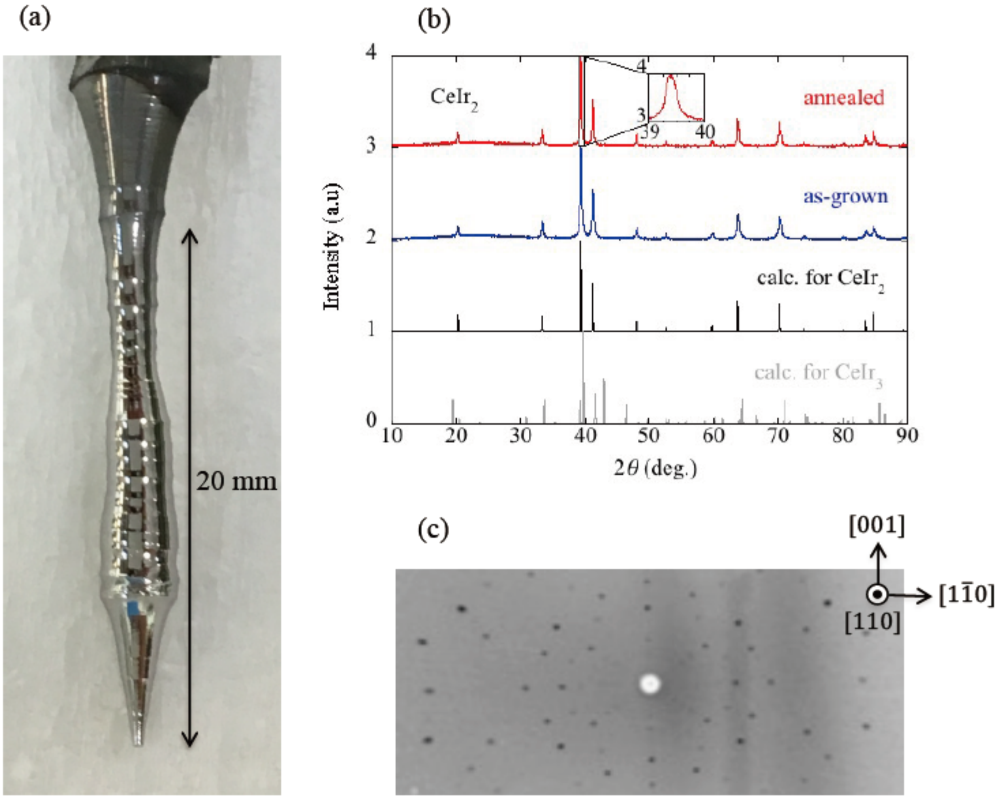
(a)
20 mm
(b)
CeIr$_2$
annealed
as-grown
calc. for CeIr$_2$
calc. for CeIr$_3$
Intensity (a.u)
2θ (deg.)
0
1
2
3
4
10
20
30
40
50
60
70
80
90
39
40
(c)
[001]
[1$\bar{1}$0]
[110]

Fig. 1

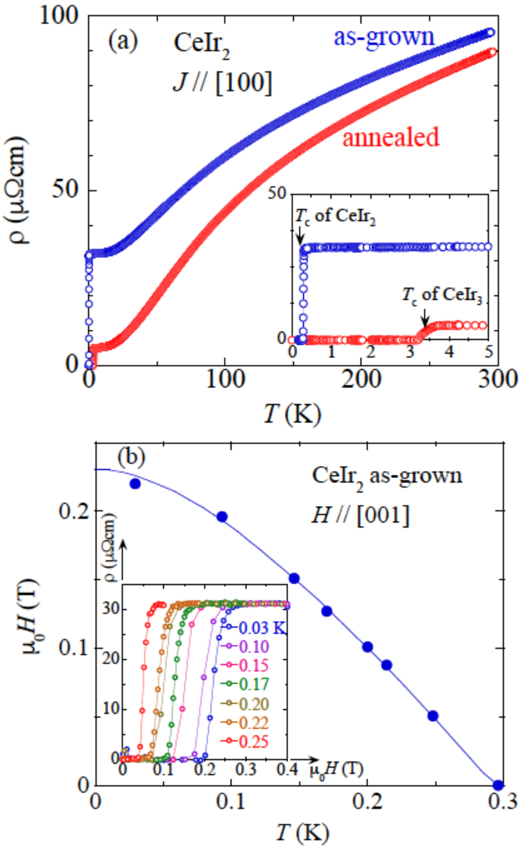
(a)
CeIr$_2$
J // [100]
as-grown
annealed
ρ (μΩcm)
T (K)
100
50
0
0
100
200
300
50
0
T_c of CeIr$_2$
T_c of CeIr$_3$
0
1
2
3
4
5
(b)
CeIr$_2$ as-grown
H // [001]
μ_0H (T)
T (K)
0.2
0.1
0
0
0.1
0.2
0.3
ρ (μΩcm)
30
20
10
0
0
0.1
0.2
0.3
0.4
μ_0H (T)
0.03 K
0.10
0.15
0.17
0.20
0.22
0.25

Fig. 2

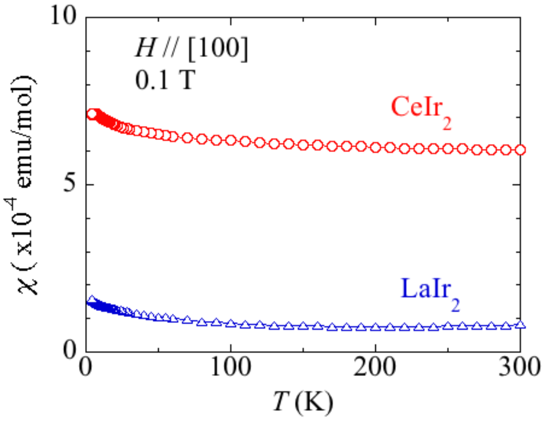

Fig. 3

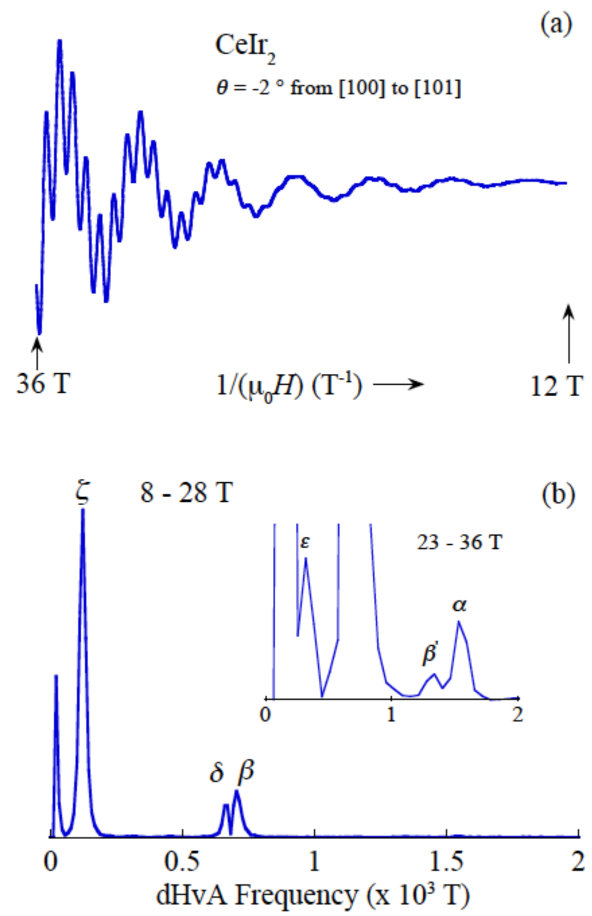
(a)
CeIr$_2$
θ = -2 ° from [100] to [101]
36 T
1/(μ_0H) (T^{-1}) ⟶
12 T
(b)
ζ
8 - 28 T
ε
23 - 36 T
α
β'
0
1
2
δ
β
0
0.5
1
1.5
2
dHvA Frequency (x 10^3 T)

Fig. 4

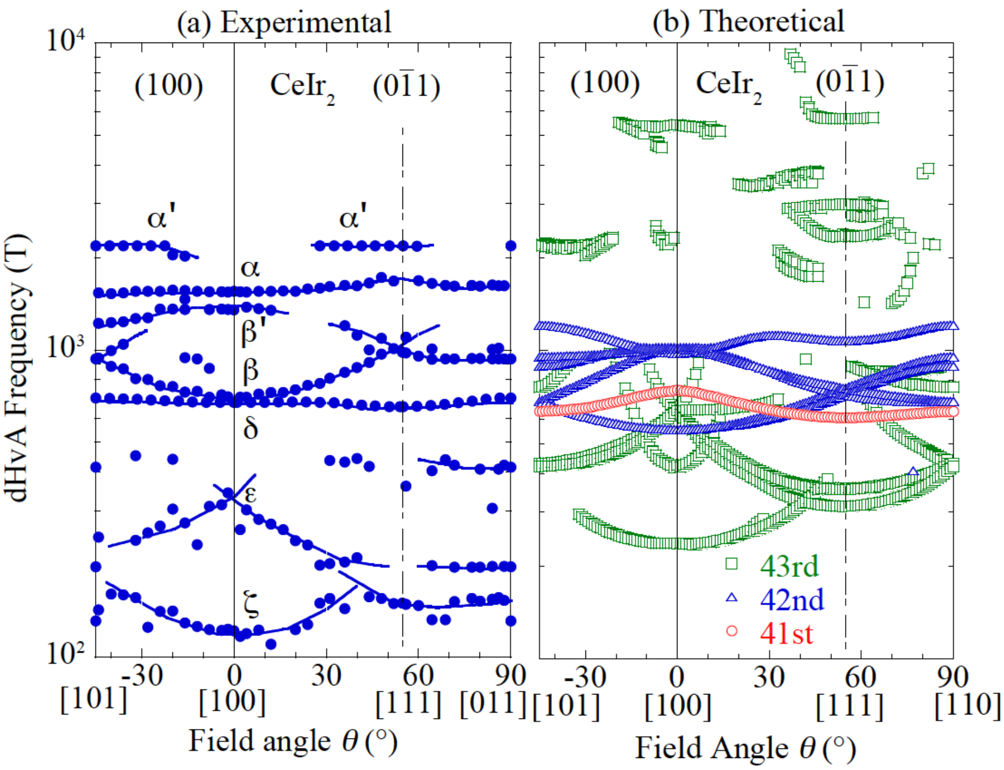
(a) Experimental
(b) Theoretical
dHvA Frequency (T)
10^4
10^3
10^2
(100)
CeIr$_2$
(0$\bar{1}$1)
α'
α'
α
β'
β
δ
ε
ζ
-30
0
30
60
90
[101]
[100]
[111]
[011]
[110]
Field angle θ (°)
Field Angle θ (°)
43rd
42nd
41st

Fig. 5

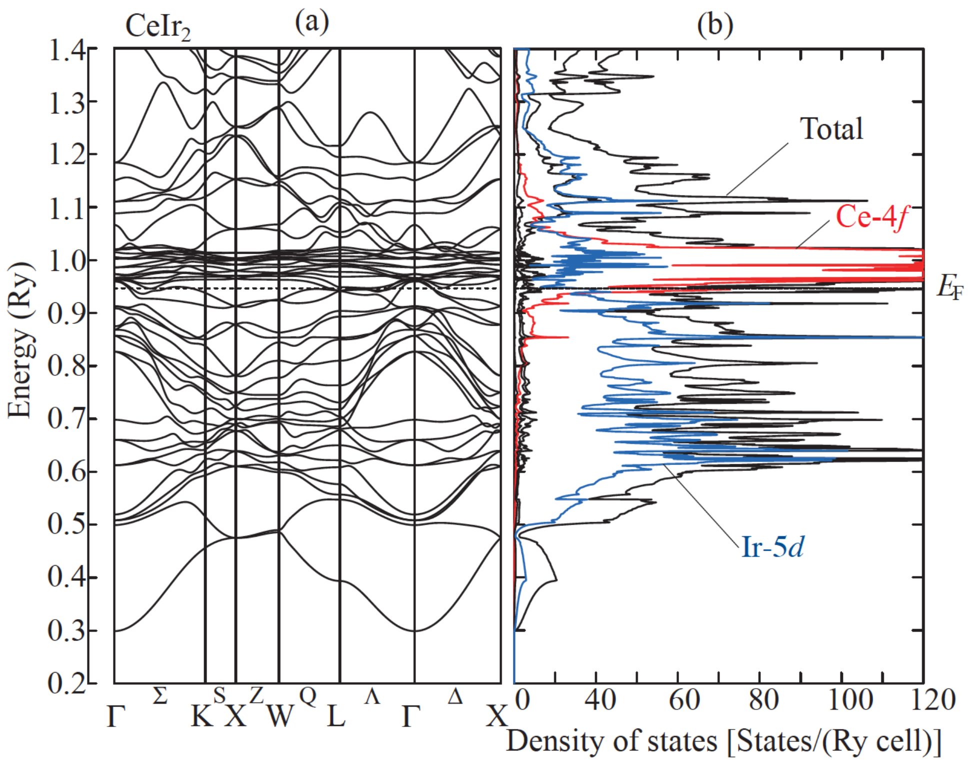
CeIr$_2$
(a)
(b)
1.4
1.3
1.2
1.1
1.0
0.9
0.8
0.7
0.6
0.5
0.4
0.3
0.2
Energy (Ry)
Γ
Σ
K
S
X
Z
W
Q
L
Λ
Γ
Δ
X
Total
Ce-4f
E_F
Ir-5d
0
40
60
80
100
120
Density of states [States/(Ry cell)]

Fig. 6

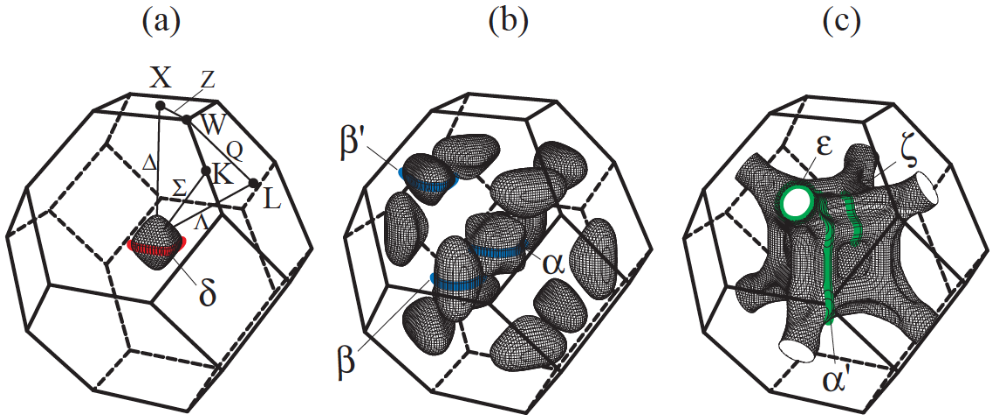

41st-band hole 42nd-band hole 43rd-band electron

Fig. 7

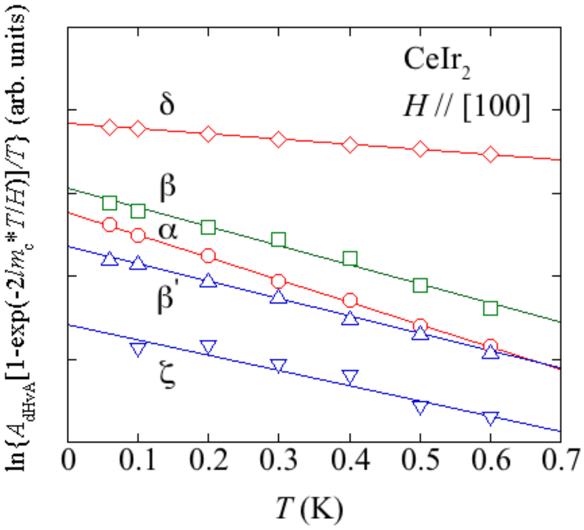
CeIr$_2$
H // [100]
δ
β
α
β'
ζ
ln{A_{dHvA}[1-exp(-2lm_c*T/H)]/T} (arb. units)
0
0.1
0.2
0.3
0.4
0.5
0.6
0.7
T (K)

Fig. 8